SANDIA REPORT

SAND97–0235 • UC–904
Unlimited Release
Printed February 1997

Adaptive Scanning Probe Microscopies

B.S. Swartzentruber, A.M. Bouchard, G.C. Osbourn

Prepared by
Sandia National Laboratories
Albuquerque, New Mexico 87185 and Livermore, California 94550
for the United States Department of Energy
under Contract DE-AC04-94AL85000

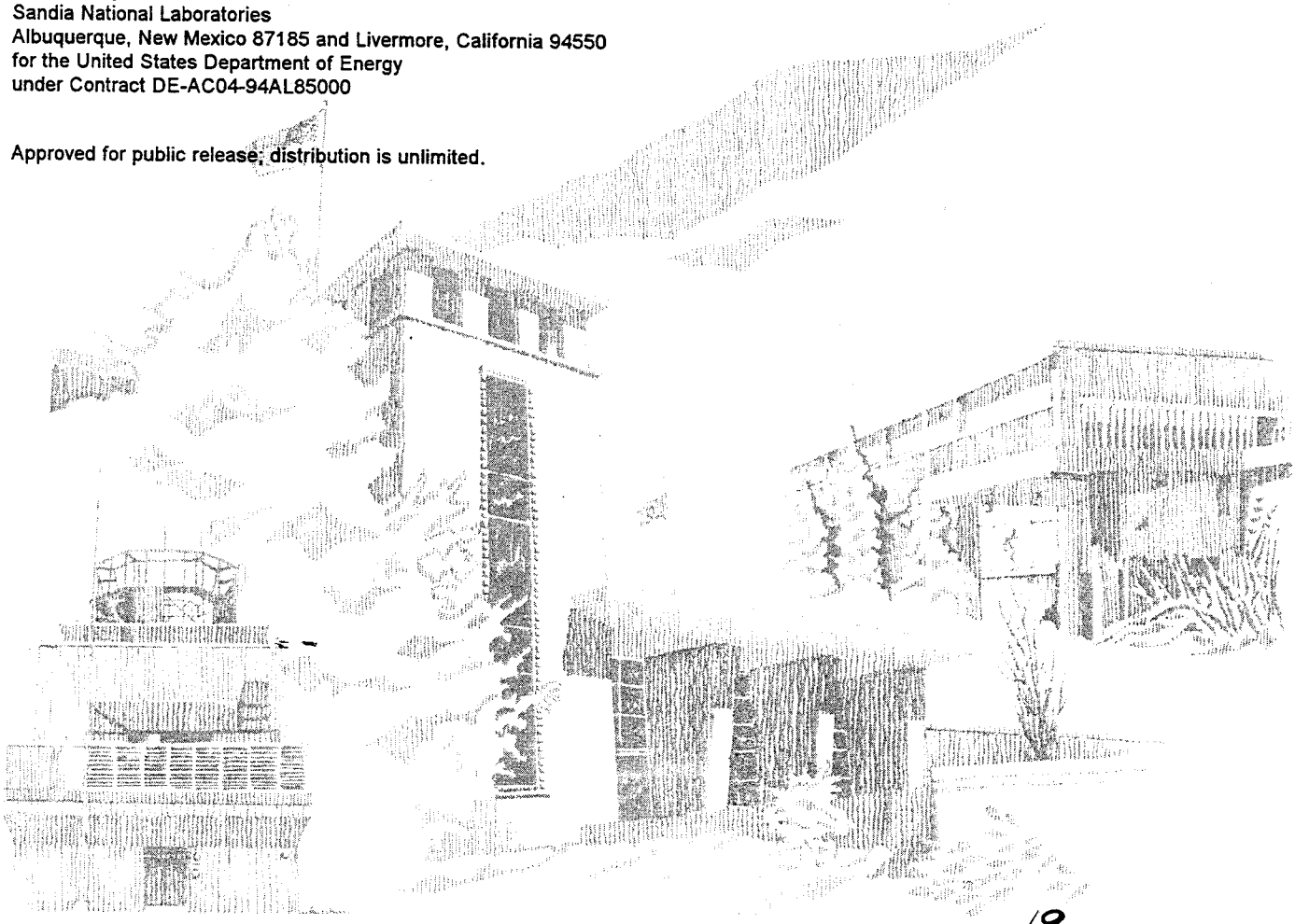

19p.

Issued by Sandia National Laboratories, operated for the United States Department of Energy by Sandia Corporation.

Available to DOE and DOE contractors from
Office of Scientific and Technical Information
P.O. Box 62
Oak Ridge, TN 37831

Prices available from (615) 576-8401, FTS 626-8401

Available to the public from
National Technical Information Service
U.S. Department of Commerce
5285 Port Royal Rd
Springfield, VA 22161

NTIS price codes
Printed copy: A03
Microfiche copy: A01

SAND97-0235
Unlimited Release
Printed February 1997

Distribution
Category UC-904

Adaptive Scanning Probe Microscopies

B. S. Swartzentruber
Surface and Interface Science Dept.

A. M. Bouchard, and G. C. Osbourn
Vision Science, Pattern Recognition & Multisensor Algorithms Dept.

P. O. Box 5800
Sandia National Laboratories
Albuquerque, NM 87185-1413

Abstract

This work is comprised of two major sections. In the first section we develop multivariate image classification techniques to distinguish and identify surface electronic species directly from multiple-bias scanning tunneling microscope (STM) images. Multiple measurements at each site are used to distinguish and categorize inequivalent electronic or atomic species on the surface via a computerized classification algorithm. Then, comparison with theory or other suitably chosen experimental data enables the identification of each class. We demonstrate the technique by analyzing dual-polarity constant-current topographs of the Ge(111) surface. Just two measurements, negative- and positive-bias topography height, permit pixels to be separated into seven different classes. Labeling four of the classes as adatoms, first-layer atoms, and two inequivalent rest-atom sites, we find excellent agreement with the *c*(2×8) structure. The remaining classes are associated with structural defects and contaminants. This work represents a first step toward developing a general electronic/chemical classification and identification tool for multivariate scanning probe microscopy imagery. In the second section we report measurements of the diffusion of Si dimers on the Si(001) surface at temperatures between room temperature and 128 C using a novel atom-tracking technique that can resolve every diffusion event. The atom tracker employs lateral-positioning feedback to lock the STM probe tip into position above selected atoms with sub-Angstrom precision. Once locked the STM tracks the position of the atoms as they migrate over the crystal surface. By tracking individual atoms directly, the ability of the instrument to measure dynamic events is increased by a factor of ~1000 over conventional STM imaging techniques.

Section I: New method for empirically determining surface electronic species from multiple-bias STM images: A multivariate classification approach.

The scanning tunneling microscope (STM) is widely used to image solid surfaces with atomic resolution. However, because STM data combine information regarding the local atomic geometry as well as the density of occupied and unoccupied states within a few eV of the Fermi energy, the specific identity of each feature is generally ambiguous. For example, in some cases "bumps" in a topograph can be identified with atomic positions, whereas in others atomic sites are actually located on topographic *minima*.

Frequently STM data are interpreted with the aid of a surface atomic structure obtained from theoretical calculations. However, the utility of the STM could be substantially enhanced if one were able to distinguish and identify different types of features directly from the STM data. In a few favorable cases, topographic images and some features of conductivity spectra have been used to infer the identity of different atomic species in a sample [1,2] or contaminants on the surface [3-6]. However, to date no *general* method of systematically identifying local atomic, electronic, or chemical species in STM images has been reported. One difficulty is that each separate species may have a complicated signature, characterized for example, by two or more peaks in conductivity at different bias values, rather than a single notable feature in the constant-current topography. Hence, two or more measurements per pixel (*i.e.*, two or more images) may be required to distinguish different species. However, faced with two, three, or many more images, all taken at different biases and conveying different visual information, it can be difficult or impossible to decipher the surface structure by visual inspection alone. The present work introduces the use of multivariate image classification techniques to accomplish this task: to distinguish and identify different electronic species present in multiple-image STM data which may be difficult or impossible to extract from the raw images by eye.

The difficulties associated with distinguishing subtle multivariate patterns in the data, and the need to identify large numbers of pixels, motivate the use of computer classification techniques. Computer analysis of multiple-image data sets is a common practice in the context of multispectral satellite imagery (see, *e.g.*, Chapter 10 of Ref. 7, and references therein), where pixels are identified according to complicated spectral signatures. Many ideas may be borrowed from the multispectral satellite literature to analyze multiple-bias STM images analogously.

The goal of systematically identifying pixels in multispectral satellite imagery can be achieved by two main approaches, unsupervised and supervised classification. In *unsupervised* classification, pixels are categorized, *i.e.*, divided into classes according to their spectral signatures. Then, in order to *identify* each class, additional information (such as "ground-truth" data, *i.e.*, identifying soil, vegetation, etc., directly at the imaged ground site) is compared with the classified results. One difficulty in using this approach directly with STM imagery is that typically the intensities in each image vary smoothly with position. Physically distinct classes are joined at boundary pixels which mix the properties of both, making a clear division between adjacent classes difficult to achieve.

In *supervised* classification, or "pattern recognition," groups of pixels, termed "training data," are selected which are *known* to belong to certain identified classes (water, soil, vegetation, etc.). Then each pixel's spectrum is compared with those of the training data to determine which class it "looks like" most. The difficulty in applying this approach to STM data is that, in

analyzing a new system, we lack the foreknowledge of class identities necessary for defining the training data.

We have developed a new approach for analyzing multiple-bias STM imagery, which has some features resembling both the supervised and unsupervised approaches used for satellite imagery, but which addresses the specific difficulties associated with STM data mentioned above. Our new algorithm cleanly divides the pixels into unidentified classes while simultaneously *finding* appropriate training data for each class. Then, the identities are determined by comparison with additional experimental data or theory. Finally, once each class has been assigned a specific identity, the associated training data can be reused to identify pixels from subsequent images, by direct pattern recognition. Using a library of known training data, the pixels of many new data sets (taken under similar experimental conditions) can be rapidly and automatically identified in the pattern recognition step.

In this section, we demonstrate the first two of the above three steps, using dual-polarity constant-current topographs to classify and identify the different electronic species on the Ge(111) *c*(2×8) surface. We choose this well-defined system to demonstrate the effectiveness of our classification algorithm in determining the correct surface structure and in identifying classes which are not obvious from visual inspection of the raw images.

As described below, pixels are separated into classes of different electronic types according to the positive- and negative-bias topograph heights, without assuming any particular atomic structure of the Ge(111) surface. With just two measurements at each pixel, the multivariate analysis enables us to distinguish seven separate classes on a single terrace. Since we are establishing a proof of principle, here, we compare the classification results with the accepted atomic structure of the *c*(2×8) reconstruction of the Ge(111) surface [8], both to validate the results and to *identify* each of the classes with a specific electronic species. If we identify four of the classes with the atomic positions of the model structure, specifically, adatoms, first-layer atoms, and two inequivalent rest atom sites, our results are in very good agreement with the accepted structure. The remaining classes, characterized by isolated topographic features which do not show the periodicity of the reconstructed surface, are identified as contaminants and/or structural defects.

Thus, much of the surface structure can be obtained empirically from a direct multivariate analysis of the STM data. This work represents the first step toward our long-term goal of developing a general tool for classifying and identifying electronic species from multivariate scanning probe microscopy (SPM) imagery.

The samples used in this study are cut from highly doped, nominally flat Ge(111) wafers. The surfaces are prepared by sputtering with 1.0 kV Ar ions followed by annealing at 800-850 C for several minutes. Upon cooling to room temperature the samples are placed on the STM. In Figs. 1(a) and 1(b), we show empty and filled state constant-current topographs of the Ge(111) surface taken at sample biases of +2.0 and –2.0 V, respectively, using 1.0 nA demanded tunnel current. The dual-polarity images are acquired

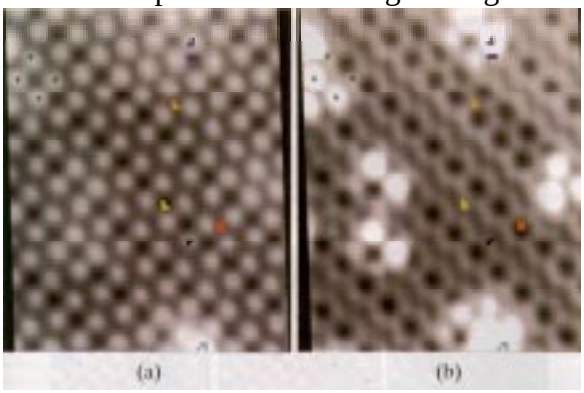

Fig. 1 Constant-current topographs of **(a)** empty states (obtained at a sample bias of 2V) and **(b)** filled states (obtained at –2V sample bias) of Ge(111). Colored pixels are first-iteration training set pixels as discussed in the text. Image scale is ~ 80×80Å^2.

simultaneously by tunneling into filled (empty) states while scanning from left to right (right to left). The spatial shift between the images due to piezo hysteresis (typically < 1%) is determined by acquiring images at the same bias in both directions and measuring their lateral displacement. Fig. 1(b) has been shifted to be in registry with Fig. 1(a).

Here, we describe the multivariate analysis procedure for a set of *k* STM images comprised of a combination of current, conductivity, and/or topography measurements acquired on a single region of the surface. All of the images are in registry, and each image is comprised of *N* pixels, each characterized by an intensity value. An alternate description of the set of *k* images is a *single* image data set where each of the *N* pixels is described by a *k*-dimensional "measurement vector" whose components are the intensities of the respective individual images at a given pixel location. The measurement vectors can also be viewed as points in a *k*-dimensional scatter diagram. For example, the gray points in Fig. 2 show the two-dimensional (2D) measurement vectors of all of the pixels in the two STM images, Fig. 1(a,b), where the intensity (tip height at constant current) of the positive- (negative-) bias image is plotted on the I_+ (I_-) axis.

The goal in the multivariate analysis is to determine what pixels can be grouped together in a class, by ascertaining what pixels have measurement vectors that group together in the scatter diagram [9]. As is clear from Fig. 2, the points are so dense and nearly continuous in the scatter diagram that it is not obvious from visual inspection how to accomplish this grouping in a reliable way. The same difficulty arises for other types of multivariate data as well, such as satellite imagery or magnetic resonance imagery.

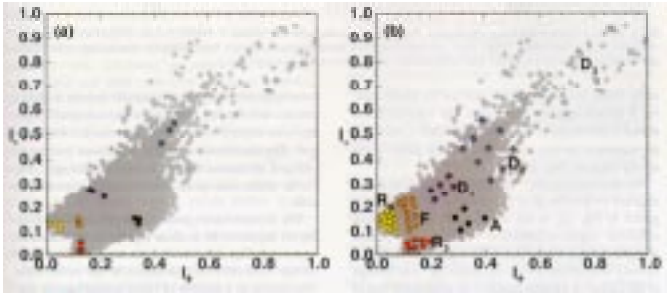

Fig. 2 Scatter plot of measurement vectors (gray points) of STM images, Fig. 1(a,b). I_+ (I_-) represents normalized intensity (topography height) in the positive- (negative-) bias image. First-iteration **(a)** and saturated **(b)** training sets for Classes 1-7 are color-coded black, red, yellow, orange, dark blue, medium blue, and light blue, respectively. Each class is labeled according to identity determined below, A (adatoms), F (first-layer atoms), R_3 (three-fold symmetric rest-atoms), R_4 (four-fold symmetric rest-atoms), D_1, D_2, and D_3 (three defect classes).

As mentioned above, STM data have some special requirements for a successful multivariate classification algorithm. First, the algorithm must provide a clear division between classes, which are typically mixed at pixels that are on the boundaries between classes, as evidenced by the continuity of points in Fig. 2. Secondly, the first analysis of a new surface must be done without knowledge of training data. Generally, it is not obvious to the eye how many classes will be distinguishable in a set of two or more images. Thus, the algorithm must be capable of determining the number of distinguishable classes automatically, rather than requiring the number of classes to be known beforehand. In addition, "unexpected" classes which arise from a departure from the ideal surface structure, such as structural defects, contaminants, or streak-like tip artifacts, should separate out naturally.

Since existing multispectral classification techniques were inadequate for the analysis of STM data, we have developed a new "bootstrap" algorithm which satisfactorily addresses each of the above concerns [10]. In the following, we describe the classification procedure generically, while demonstrating it in the context of analyzing the STM images shown in Fig. 1.

First, we select a few pixels that we can reasonably assume belong to the same class. Specifically, we choose nearest-neighbor pixels localized on a notable single feature of one of the images, *e.g.*, three pixels in the center of a "bump" in the empty-state topograph, as indicated in black in Fig. 1(a). We assume that the entire bump is a single object, and that the pixels making it up belong to the same class. The selected pixels define a first-iteration training set for Class 1, and their measurement vectors are shown by black points in the scatter diagram, Fig. 2(a).

We then compare the "test set", *i.e.*, the set of measurement vectors for all of the pixels in the image (gray points in Fig. 2), to the training set, using a visual empirical region-of-influence (VERI) [11] pattern recognition algorithm. The VERI algorithm computationally determines which test points lie near enough to the cluster of training points to be considered part of the cluster by human visual perception. A detailed discussion of the VERI algorithm is provided in Ref. 11. The points which are considered to cluster with the training points are then considered to belong to Class 1 and are color-coded black. All others, termed "outliers", are as yet unclassified; these remain color-coded gray. The classification results for the black training set of Fig. 2 are shown in the "classification image" Fig. 3(a), in which each pixel is color-coded according to class.

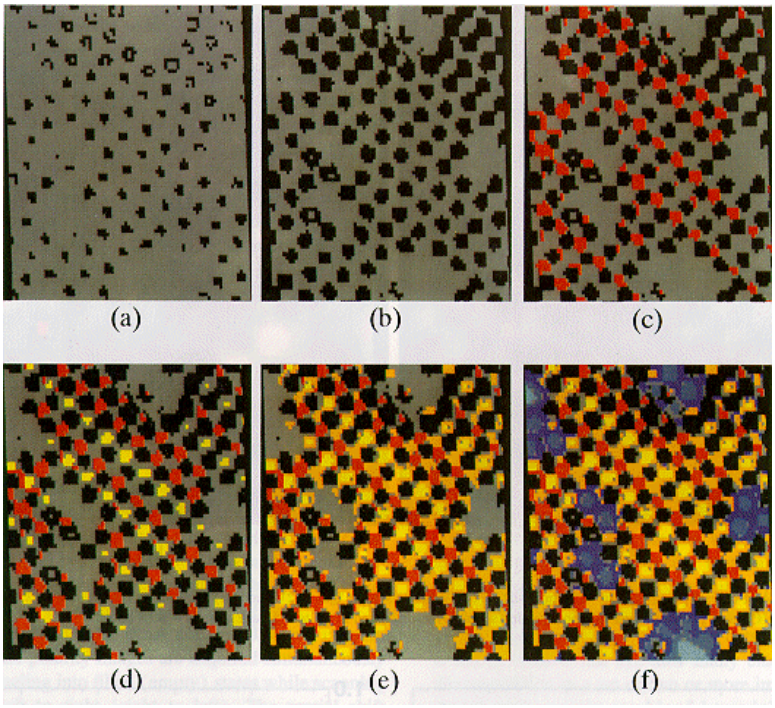

Fig. 3 Results of multivariate image classification. Pixels are color-coded according to class: 1 (black), 2 (red), 3 (yellow), 4 (orange), 5 (dark blue), 6 (medium blue), 7 (light blue), and outliers and class-boundaries (gray). Results from **(a)** first-iteration training set for Class 1, and for saturated training sets for **(b)** Class 1, **(c)** Classes 1 and 2, **(d)** 1-3, **(e)** 1-4, and **(f)** 1-7.

The measurement vectors of the first-iteration training set happen to be so close together in measurement space (see Fig. 2(a)) that they do not provide a broad enough collective representation of the entire class. This results in a number of other similar bumps elsewhere in the image failing to be classified as Class 1, as indicated by the sparseness in Fig. 3(a). We therefore iteratively refine, or "bootstrap", Class 1 as follows: (i) A new (second-iteration) training set of pixels is selected from among those already found to belong to the class (*i.e.*, that are already color-coded black), but which are more broadly distributed in measurement space. In a measurement space which is 2D (or 3D), this can be achieved manually, by selecting points in measurement space which are of approximately uniform density within the larger cluster of Class 1 points. Alternatively, one can select Class 1 pixels from different spatial regions of the image, and inspect the measurement space to ensure that such points are approximately uniformly distributed within the Class 1 cluster. However, in higher dimensions, the measurement space is not accessible to visual inspection, so an automated method for redistributing the next iteration training set is under development. (ii) Then the test set is classified again with the VERI

algorithm using the new training set. Steps (i) and (ii) are then repeated. The number of pixels belonging to the class monotonically increases and the class in real space smoothly fills in (see Fig. 3(b)).

The iteration procedure is complete when the number of pixels in the class saturates, and successive iterations effect no appreciable change on the class. We retain the "saturated training set" for Class 1 for further analysis of the image. In some cases, the procedure initially smoothly saturates, but then a discontinuous jump occurs, resulting in a dramatic increase in classified pixels, when a boundary to another class is inadvertently crossed. This discontinuity is unmistakable, because the real-space classification image changes modestly with iterations as saturation is being approached, and then undergoes a sudden dramatic qualitative change. Indeed, we can use this dramatic image change to our advantage, to probe the class boundaries in measurement space. By determining what part of measurement space is associated with the newly, obviously improperly classified pixels, we can adjust the next iteration training set to exclude those pixels, *i.e.*, by selecting training points farther from the boundary. The saturated training set for Class 1, associated with the results of Fig. 3(b), is shown by the black points in Fig. 2(b).

After bootstrapping Class 1, we choose a first-iteration training set for Class 2 by selecting a set of nearest-neighbor pixels among those still unclassified. The Class 2 training set can be chosen based on either a notable feature in the original images or some notable collection of outlier pixels in the classification image, *e.g.*, a periodic arrangement of unclassified pixels, or a "hole" in an otherwise periodic arrangement of classified pixels. In the present investigation, we choose four pixels centered in one of the hexagonal rings of the filled-state image, as shown in red in Fig. 1(b). The corresponding measurement vectors are also shown in red in Fig. 2(a). The entire test set is then classified according to a combined training set consisting of the saturated training set for Class 1 (black points in Fig. 2(b)) and the new training set for Class 2. Then keeping the Class 1 training set fixed, Class 2 is bootstrapped in the same manner as Class 1. The results are shown in Fig. 3(c), where now Class 2 is shown in red, and the associated saturated training set is shown as red points in Fig. 2(b).

This procedure of selecting a first-iteration training set and then bootstrapping a new class is repeated until essentially all pixels have been classified. We choose Class 3 from a valley with four-fold symmetry in the empty-state topograph, as indicated by the yellow pixels in Fig. 1(a). The first-iteration training set, saturated training set, and saturated results are indicated by yellow in Figs. 2(a), 2(b) and 3(d), respectively. Note that the three-fold symmetric valleys in Fig. 3(d) are as yet unclassified, so Class 4, indicated in Figs. 1(a), 2, and 3(e) by orange, is naturally selected from those. It turns out that, in addition to the three-fold symmetric sites, many unclassified pixels surrounding yellow features in Fig. 3(d) are filled in with orange in Fig. 3(e). We remark that no prior knowledge of the specific atomic surface structure is necessary to select the starting pixels for each class. We use only visual cues, such as local maxima or minima, symmetry sites, or holes in the classified image, to guide our choice of first-iteration training sets for discerning new classes.

Note the isolated regions of unclassified pixels in Fig. 3(e), which breaks the underlying periodicity of the first four classes. Classes 5, 6, and 7 are selected from among these "holes" in the classification image in the same manner as the first four classes. The first-iteration training-set pixels and measurement vectors for classes 5, 6, and 7 are indicated by dark, medium and light blue, respectively, in Figs. 1 and 2(a). The saturated training sets are similarly displayed in

Fig. 2(b), and the final classification image is shown in Fig. 3(f). As discussed further below, the last three classes are associated with structural defects and/or contaminants, and are naturally separated from the rest of the surface by this bootstrapping approach. Very nearly all of the pixels in Fig. 3(f) are classified, signaling that the classification is complete, with a total of seven classes distinguished.

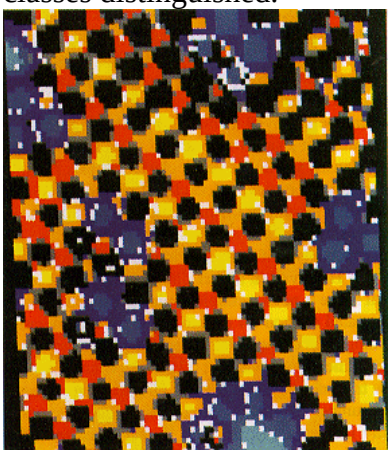

Fig. 4 Results of multivariate image classification for Classes 1-7, color-coded as in Fig. 3(f), except with class-boundary pixels shown in white. Note that the pixels with measurement vectors on class boundaries in measurement space tend to lie on the boundaries between classes in real space.

Generally, there will be some measurement vectors lying on the boundaries between classes which cannot be unambiguously classified as one or the other adjacent class. That is, they are sufficiently close to the training points of both classes that they could be said to belong to either class. However, such ambiguous pixels are not problematical for our bootstrapping approach. Although they themselves have no unique class identity, they do not blend the two adjacent classes into a single class. Further, in the real-space classification image, they lie on boundaries between classes, as is seen in Fig. 4, in which class-boundary pixels are color-coded white. Since their identity as class boundaries does not really add information, in Fig. 3 they are color-coded gray to minimize added confusion, as compared to Fig. 4.

Although we have achieved the separation of the image into classes, the electronic or atomic *identity* of each class remains to be determined. To identify classes with a specific electronic or atomic species, the classification results can be correlated with other experimental data (analogous to ground-truth data in satellite imagery classification), theory, or classification results from a related surface. In the present demonstration for a well-characterized surface, we compare the final results of Fig. 3(f) with a schematic ball-and-stick model of the *c*(2×8) reconstruction of the Ge(111) surface [8] shown in Fig. 5(a). However, if a theoretical model of the atomic structure were unavailable, data from appropriately designed experiments or previous classifications could be used to identify classes. Indeed, classification results can be used to develop or confirm models for poorly understood surfaces. Additionally, a library of identified classes can be developed to facilitate the analysis of frequently studied or closely related surfaces.

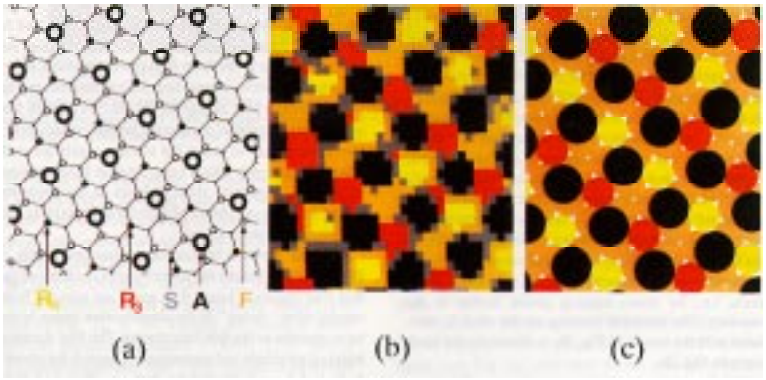

Fig. 5 **(a)** Ball-and-stick model of Ge(111)*c*(2×8) atomic structure, after Ref. 8. Large open, large solid, small open, and small solid circles correspond to adatoms (A), rest-atoms (R_3 and R_4, depending on the number of nearby adatoms), first-layer atoms (F), and second-layer atoms (S), respectively. **(b)** Reproduction of the center periodic region of Fig. 3(f); results of multivariate classification. **(c)** Reproduction of (a) with larger "atom" sizes, and atomic sites color-coded to represent the identifications with classes in (b): adatoms (A, black), three-fold rest-atoms (R_3, red), four-fold rest-atoms (R_4, yellow), first-layer atoms (F, orange).

Fig. 5(b) represents a small periodic portion of the classified image Fig. 3(f). The classification results correlate well with the model if we identify black with

adatoms, orange with first-layer atoms, and red and yellow with rest-atoms at two inequivalent symmetry sites, R_3 or R_4, that have either three or four neighboring adatoms, respectively. Second-layer atoms, which appear in the model structure, are not seen in our results. This means that, with the measurements used here, second-layer atoms do not display a signature distinct from the other four classes, at least with the pixel size used. For ease of comparing the model with the classified results, we re-display the *c*(2×8) model in Fig. 5(c), with the balls color-coded to represent the identifications with the classes in the analyzed image and increased in size to fill space. Viewed in this way, the similarity between Figs. 5(b) and (c) is striking, lending support to our atomic site identifications.

Classes 5, 6, and 7 (dark, medium, and light blue, respectively) are atypical of the periodicity of the surface, and are associated with structural defects or contaminants. The three-lobe features at the right and left edges of Fig. 3(f) are attributed to a structural defect of local $\sqrt{3}$ symmetry at the domain boundary of several *c*(2×8) domains [8]. The four-lobe features near the top and to the left of the center of Fig. 3(f) arise from a type of defect that has previously been shown to be associated with adsorbed hydrogen [3] or substitutional group-III dopant atoms [4] both of which inhibit charge transfer from the adatoms to the rest atoms. The features at the bottom and upper left corner of Fig. 3(f), the only ones containing Class 7 (light blue) pixels and showing up as bright spots (very high peaks) in both topographs Fig. 1(a,b), we interpret as being extra atoms sitting above the level of the rest of the surface. In the current study we cannot determine the specific nature of the impurities, but hope that more detailed experiments may be of use in determining their identity.

Several aspects of the classification results of the Ge(111) surface are not obvious from either the raw STM images (Fig. 1) or the *c*(2×8) model (Fig. 5(a)). Both the rest atom sites, R_3 and R_4, sit at the same height in the atomic model and have three bonds to second layer atoms, yet they are electronically inequivalent, according to the classification of these dual-bias images. Since we can distinguish between rest atom sites of different symmetry, one might expect a similar ability to distinguish between adatom sites of different symmetry, having either three or four neighboring rest atoms. Yet, according to the dual-bias STM measurements, the two adatom sites are electronically equivalent. From the raw images, it is difficult to identify visually any notable features as first-layer atoms, *i.e.*, no particular bumps or dips, whereas the bootstrap algorithm does enable us to distinguish first-layer atoms as a separate class. Thus, the classification procedure does extract information from the raw images which is not obvious to the eye, and also provides information different from that in the atomic structure model, since the classification is according to electronic signature, rather than purely topographical.

We emphasize that the classification results do depend on the measurements used, so different (or more) measurements may, for example, permit the distinction between adatom sites, or the distinction of a second-layer atom class. However, preliminary work with multiple-bias conductivity images reveals that many choices of measurements over the same region can yield similar classification images. That is, different choices of measurements have not produced radically different results, so that we can be confident that our results will not be totally arbitrary, depending on the choice of measurements.

We have found our bootstrap algorithm to be very robust, provided a few obvious errors are avoided. (i) The first-iteration training set of any class *must* consist of pixels which all belong to a single class. If one inadvertently combines classes in the first iteration, there is no hope of separating them with further iterations. For example, suppose we select single pixels

from the center of each of four bumps that appear identical in Fig. 1(a) and use them as a first-iteration training set for Class 1. Such a set of pixels is displayed in green in Fig. 1(a), and the corresponding pixels in Fig. 1(b) are also displayed in green. Even though in Fig. 1(a) they appear to belong to the same class, if we examine Figs. 1(b) and 3(f), we see that the green pixels actually include both Classes 1 and 6. By incorrectly assuming that all of the spatially separated green pixels belong to the same class, we would inadvertently combine the black and medium blue classes of Fig. 3 together into one. This is why we consistently use nearest-neighbor pixels for first-iteration training sets: it is safer to assume that they do legitimately belong to the same class. (ii) Similarly, if pixels on a boundary between classes are selected for a first-iteration training set, both adjacent classes will be joined into a single class. This error is easily spotted, since typically an unexpectedly large number of pixels will be labeled as the new class on the first iteration, *i.e.*, the result is not sparse, as in Fig. 3(a). For STM images, class-boundary pixels are most often in regions of large slope. Local maxima, minima, and saddle points are safe choices for first-iteration training sets. (iii) Finally, if a discontinuous jump occurs during the bootstrapping of a particular class, this signifies that an additional (but distinguishable) class has been inadvertently joined to the current one. The next iteration training set must be adjusted to retain only the single class to achieve valid results.

If these visually obvious warnings of error are heeded, we find that many different choices of first-iteration training sets give similar results. We have bootstrapped the classes in a different order, also obtaining classification images visually similar to Fig. 3(f). Applying the same procedure to other dual-bias images of the Ge(111) surface also yields equivalent results. In fact, even an attempt to *force* the procedure to yield an incorrect classification image, by asymmetrically spreading the training data in measurement space at each iteration to add some incorrect pixels to the class, resulted in the obvious discontinuous jump in pixel number characteristic of crossing a class boundary. Thus, as long as the warnings (i)-(iii) are heeded, the bootstrap algorithm proves very robust.

By selecting training sets for each class one at a time, we obtain a clear division of the training points in the 2D measurement space (Fig. 2). Note, however, that the classes do not separate along either single dimension. For example, if the pixels were classified only according to their value of I_-, then Classes 1 (black), 3 (yellow), and 4 (orange) would blend into a single class. Similarly, if they were classified by I_+ alone, Classes 2 (red) and 4 (orange) would combine into a single class. *Both* measurements, I_+ and I_-, are required to separate the classes. This is a key idea for multivariate classification in general and specifically for the classification of STM images: a single measurement (image) is likely to be insufficient to separate all classes that are present.

We remark that this bootstrapping approach cannot be used with all pattern recognition techniques. The technique must be capable of distinguishing outliers and class-boundary pixels reliably, as does the VERI algorithm developed in Ref. 11. Furthermore, caution is warranted in applying standard unsupervised techniques to this type of image analysis, as class-boundary and outlier pixels often lead to visually unreasonable class groupings. For example, ISODATA [12], one of the "smartest" and most commonly used unsupervised classification algorithms, results in a real space classified image that does not correlate well with the atomic model. In addition, the number of classes is required as an input parameter, and for all of the numbers of classes we tried, from four to thirty, the algorithm gives a similarly poor performance.

The dependence of a classification on the details of the STM tip is an issue of some concern. We carried out the procedure described above for Figs. 2 and 3, on another region of the same sample but under different tip conditions, and got similar results. However, STM generally convolves the tip and surface electronic structures, so significant tip switches may be problematical in some cases. Successfully dealing with tip differences will be of great importance in developing a library of identified electronic species whose training sets we would want to be transferable across different experiments, for rapid pattern recognition of new data. The effect of tip differences on electronic species' signatures is the subject of a separate investigation.

In the present study we have used dual-polarity constant-current topographs for classifying pixels on a surface comprised of a single atomic species. Classifying more complicated surfaces using either similar measurements, STM conductivity images, or other SPMs with multivariate signals should also be possible. However, we anticipate new challenges in classifying higher-dimensional data as compared to the current dual-polarity case. A general but counter-intuitive property of multivariate classification algorithms is that redundant information, in the form of too many measurement vector dimensions, can actually make the classes *less* distinguishable in measurement space. When the number of images is large, care must be taken in choosing the measurements used to classify the image, so as to retain valuable information, but remove redundancy. In addition, a higher dimensional measurement space cannot be visually inspected as can a 2D (and possibly 3D) space, such as Fig. 2, making it more difficult to choose training sets and verify that they separate out in measurement space. Preliminary work with STM multiple-bias conductivity images suggests that these can be used to classify surfaces, although we have yet to determine whether such measurements prove much more useful than the simpler dual-bias measurements.

We have demonstrated the multivariate classification of the electronic structure of the Ge(111) surface from dual-polarity STM images. With only two measurements, the technique distinguishes seven different classes on a single terrace. If we identify adatoms, first-layer atoms, and two inequivalent rest-atom sites (R_3 and R_4) from among the classes, we find that the classification results agree very well with the accepted structure of the *c*(2×8) reconstruction of Ge(111). The remaining classes are associated with structural defects and contaminants. Thus, multivariate image classification extracts much of the electronic structure directly from the STM data that is not obvious to the eye from the images alone.

Our bootstrap method yields a meaningful division of classes, even though their edges are joined together in measurement space by pixels lying on the boundaries between classes. With this method, defects are also naturally revealed, as a class of isolated pixel regions which remain unclassified after the periodic structure of the surface is filled in.

The key is using more than one measurement to separate classes in a multidimensional measurement space. In the present work we have used dual-polarity STM images. Preliminary work with multiple-bias conductivity images indicates that subtle differences (on the order of a few percent) in conductivity peak heights can be sufficient for distinguishing physically meaningful classes in the images. The real utility of the method will be in distinguishing different electronic species whose signatures are too complex and whose differences are too subtle to distinguish visually. The goal is to establish a library of training data of identifiable electronic or atomic species from SPM images, for rapid classification of surfaces composed of recognizable species in the library. Such topics are beyond the scope of this article, but are

important future steps toward our goal of developing a general electronic/chemical classification/identification tool for SPM imagery.

Section II: Direct measurement of surface diffusion using atom-tracking scanning tunneling microscopy.

The evolution of surface morphology during growth or etching depends on the detailed interplay between a myriad of atomic-scale kinetic processes. In order to control particular surface morphologies (*e.g.*, to suppress or enhance over-layer island formation) it is important to achieve an understanding of the balance between thermodynamics and various kinetic processes. The equilibrium surface morphologies are controlled by thermodynamics, that is, the binding or configurational free energies, while the rates at which dynamic events occur on the surface are controlled by the details of the activation barriers -- kinetics.

To study the evolution of surface morphology investigators often utilize rate-equation analysis [13], Monte Carlo [14], or molecular dynamics simulations [15] which explicitly require the input of specific atomic-scale energy parameters. The values for the input parameters are derived in a variety of ways ranging from first-principles total energy calculations, through semi-empirical calculations, *e.g.*, from the embedded-atom method, to purely empirical values chosen to reproduce particular measured morphological features. Of course, the ideal parameter values are derived from quantitative experimental measurements of particular system-specific atomic-scale processes. The quantitative measurements of individual atomic-scale energy parameters not only serve as inputs to realistic simulations and model calculations, but also enable the validation and refinement of such calculations. Such processes on certain metal systems have been studied for some time using field ion microscopy [16].

Because of its inherent atomic-scale resolution and access to a broad range of materials the STM is ideally suited to studies of individual atomic-scale processes on surfaces -- particularly since the advent of variable-temperature versions which enable the imaging of the surface as the rate of specific processes are varied by altering the sample temperature. However, conventional STM image acquisition is limited by the rate that dynamic events can be resolved. In this section we report on the use of a novel atom-tracking technique that allows direct quantitative measurements of the diffusion of adsorbed silicon dimers on the Si(001) surface from room temperature to 128 C over which the diffusion rate changes by four orders of magnitude. The groundwork for this investigation was laid in several recent studies of the structure and stability of silicon deposition on Si(001) in the low coverage limit [17-19].

The experiments are performed in an ultra-high vacuum chamber with a base pressure of 8×10^{-11} torr that contains the STM and an evaporative silicon source. The clean surfaces are prepared by annealing the samples to 1250 C for several seconds and then cooling to room temperature [20]. To evaporate silicon atoms onto the clean, cooled surface a nearby silicon wafer is heated to ~1150 C and an intervening shutter is opened for 3-5 seconds resulting in the deposition of about 1 percent of a monolayer of silicon atoms.

When individual silicon atoms are deposited onto the surface at room temperature they diffuse rapidly and readily find another atom with which to form a stable cluster, *i.e.*, an ad-dimer. As can be seen in Fig. 6(a) these ad-dimers appear as bright bumps in the STM images. Some workers argue that the most energetically favorable location for the ad-dimers is to sit *between* the substrate dimer rows [17]. However, the majority of the ad-dimers formed on a

room temperature substrate sit in metastable sites *on top* of the dimer rows, presumably due to the details of the kinetic pathway through which they are formed [17-19]. Examples of on-top and between-row clusters are indicated in Fig. 6(a) by the solid and dashed circles respectively.

The design of our microscope allows the repeated imaging of the surface at elevated temperatures enabling the measurement of atomic-scale dynamic events through the comparison of consecutive images [21,22]. Figures 6(a,b) show two images acquired at 65 C taken 29 seconds apart. The displacement of the ad-dimers along the top of the rows can be seen between the images [23]. An example is circled in black. At this temperature the between-row clusters are not observed to diffuse on the time scale of many minutes, nor do the diffusing on-top site dimers fall off into the between-row sites. The highly anisotropic diffusion of the on-top ad-dimers along the substrate dimer rows was previously studied at this temperature by Dijkkamp *et al*. [24].

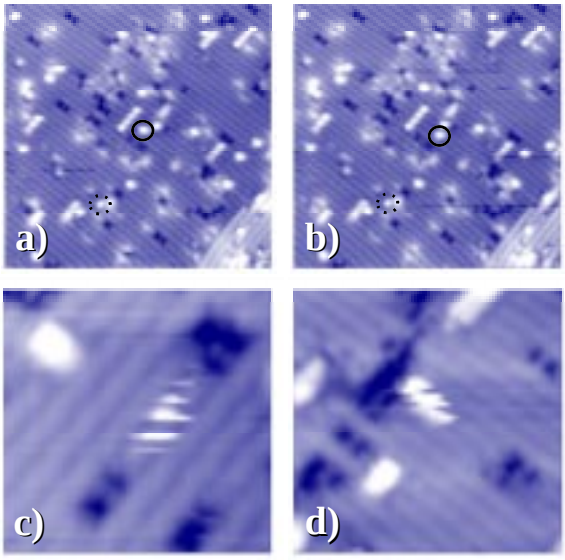

Fig. 6 High-temperature STM images of diffusing Si ad-dimers. **(a)-(b)** At 65 C diffusion is observed as displacements of the ad-dimers in sequential images (example in solid circle). Clusters between the substrate rows are comprised of more than 2 atoms. They are stable and do not diffuse (dashed circle). Scale ~250 Å. **(c)** ~70 Å and **(d)** 95 Å images taken at 128 C of two different ad-dimers trapped between substrate defects.

In the earlier anneal and quench experiments in which samples were heated for a fixed amount of time and then cooled to room temperature before imaging, Zhang *et al*. [17] and Bedrossian [18] observed that after annealing the sample at ~125 C the barrier for an on-top site ad-dimer to fall into the between-row sites is surmounted and on the time scale of several minutes the majority of clusters are observed in the between-row sites. In images acquired *at* 128 C for the present study, the vast majority of clusters are also observed to be located in the stable between-row sites, or else in compact overlayer islands. Although most of the ad-dimers have found the stable binding sites an occasional ad-dimer is observed that remains in the sites on top of the dimer rows. Figures 6(c,d) show two images acquired at 128 C of different ad-dimers diffusing on top of the substrate dimer rows. Each ad-dimer is trapped between two substrate defects that behave as repulsive hard walls. That these ad-dimers are observed and remain stable even after several hours at high temperature suggests that the simple transition from on-top site to between-row site has, in fact, a rather high barrier, and that a much lower barrier may exist that is mediated by surface defects or other neighboring clusters. The majority of the ad-dimers that are initially on top of the dimer rows may take this easy road to the minimum energy sites as they find neighboring atoms, clusters, or defects, leaving a small percentage, that are isolated from defects, stuck in the on-top sites.

The limitations of the conventional type of data acquisition are immediately apparent in Figs. 6(c,d). The images are acquired as a raster -- scanned line by line -- starting at the bottom of the image and moving to the top. For these specific 64×64 pixel images, the process takes 7.8 s to complete a frame, or 0.12 s per scan line. The diffusing ad-dimer is moving much more rapidly than the time scale of the data acquisition and therefore its exact position cannot be

defined within the images. The finite time response of image acquisition puts an upper bound on the temperature at which well-defined dynamic events can be measured -- above this temperature the events are just occurring too rapidly. The primary cause of the inadequate time resolution in measuring, for example, the diffusion of the ad-dimers is the fact that during image acquisition the STM is spending most of the time *not scanning the ad-dimer at all*, but rather simply scanning the substrate away from the ad-dimer. Of course, the time scale can be decreased by zooming in and scanning a smaller area around the ad-dimer, however, this is limited because diffusion events quickly remove the ad-dimer from the field of view.

In order to quantitatively measure the diffusion kinetics of the ad-dimers, these limitations were overcome through the development of an atom-tracking technique in which the STM tip is locked onto a selected ad-dimer using 2-dimensional lateral feedback. Once locked, the feedback electronics maintain the tip over the cluster tracking its coordinates as it diffuses over the substrate. This procedure is accomplished by dithering the tip in a circle over the surface [25]. The quadrature output of a lock-in amplifier reading the tunnel current yields, independently, the X and Y local slopes of the surface, which in turn are the input error signals to the X-Y lateral integrating feedback circuits [26]. Thus, this feedback maintains a lateral position of zero local slope -- the top of the ad-dimer is tracked by continually "climbing uphill" [27]. In the atom-tracker mode, the STM spends *all* of its time measuring the kinetics of the selected ad-dimer. When a diffusion event occurs the atom tracker quickly relocates to the ad-dimer's new position [28]. By utilizing atom tracking, the ability of the STM to resolve individual dynamic events is increased by about three orders of magnitude. Additionally, the measurement of every diffusion event eliminates the need to assume random walk statistics as is the case in mean square displacement measurements. In fact, the diffusion statistics can be measured explicitly.

In STM measurements of kinetic processes, one must be wary of altering the surface dynamics through the presence of the probe, for it is well known that the interactions present in the tunnel junction between the probe tip and the sample can be used to physically manipulate adsorbed atoms and molecules on the surface [29]. This is a particular concern in the type of measurements presented here in which the tip is restricted to a specific sample region of interest. All of the data presented below were acquired with tunneling biases between -2.5 and +2.5 volts at 0.05 nA. Over this range of parameters, no variation of the diffusion kinetics of the ad-dimers could be detected.

The atom track data consist of the X, Y and Z feedback coordinates as a function of time. Figure 7(a) shows a scatter plot of the complete set (11,300 points) of lateral coordinates of the ad-dimer in the middle of Figs 6(a,b) (circled in black) acquired at 65 C over 540 s. During the course of the measurement the ad-dimer visited 7 lattice sites along the top of the substrate dimer row, making 41 hops. The individual lattice-site visitations are easily distinguishable in the scatter plot and are separated by the Si(001) lattice spacing of 3.84 Å. The data points at each lattice site group to <1 Å, considerably smaller than the images would suggest, indicating how well the atom tracker locates the average

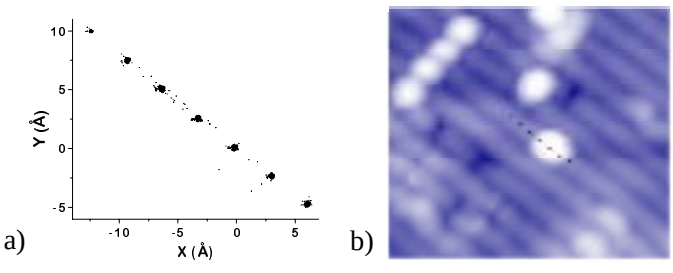

Fig. 7 **(a)** X-Y Scatter plot of data acquired at 65 C. **(b)** Superposition of the data on the STM image taken immediately before atom tracking showing the initial location of the ad-dimer.

position of the ad-dimer. This is particularly apparent when the scatter plot data are superposed on the topographic image taken immediately before atom tracking (Fig. 7(b)).

As described above, at 128 C the ad-dimers do not sit still long enough to be captured in a conventional image; however, the atom tracker easily locks-on to them. In Fig. 6(d) there are 11 lattice sites between the hard-wall defect barriers on which the ad-dimer is confined to move. The amount of time that the ad-dimer is observed on each lattice site is determined by the relative free energies of the sites. In a histogram of the site occupation probabilities (Fig. 8) it is clear that although the probability of finding the ad-dimer in one of the sites in the middle is approximately constant, the two end sites at the defects are occupied 2-3 times less frequently. The free energy of an ad-dimer on these two sites is ~20-35 meV higher than the others. A portion of this energy is probably attributable to the strain field in the lattice associated with the details of the defect structure. In this particular case only the end sites are appreciably affected. Other atomic configurations of the hard-wall defect barriers show different effects. In this context, the diffusing ad-dimer is a local probe of the atomic-scale substrate potential.

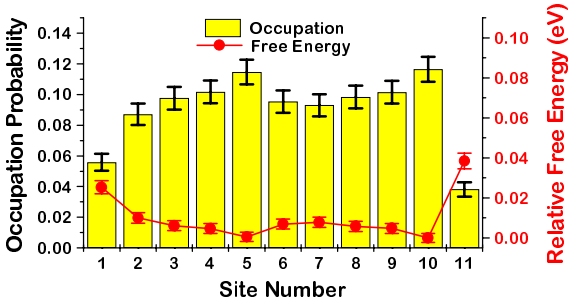

Fig. 8 Atom-track data taken at 128 C. Site occupation probabilities and the extracted relative free energies of the 11 sites are measured from 6 data sets, total time is 196 s. Error bars reflect the statistics related to the number of hops at each site.

The frequency with which the ad-dimers hop is determined by the details of the activation barrier for diffusion. The hop frequency is measured by analyzing the ad-dimer coordinates as a function of time. Two of these time-line plots are shown at the top of Fig. 9 acquired at 65 C for 538 s and at 128 C for 22 s respectively. The mean residence time (time between hops) decreases from 13.1 to 0.11 seconds as temperature is increased. In the higher temperature data there are enough hops to extract a statistically significant residence-time probability distribution, shown at the bottom of Fig. 9 (taken from a data set with 736 hops over 79 s). The dots are the measured values and the solid line is an exponential with a decay constant equal to the measured mean residence time, τ. The quality of this comparison plot is indicative of a simply activated process, *i.e.*, $1/\tau = \nu_0 \exp(-E_a/kT)$. The activation barrier, E_a, is measured as the slope of the Arrhenius plot of the logarithm of the transition rate versus 1/kT. From the hopping rates measured at several points between 25 and 128 C (Fig. 10) the diffusion barrier for silicon ad-dimers on the Si(001) surface is determined to be 0.94±0.09 eV [30]. This activation barrier for diffusion along the top of the substrate rows is higher than that measured for Si monomer

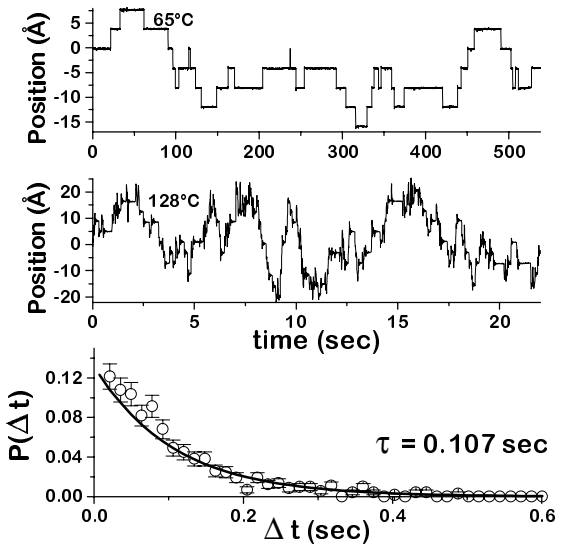

Fig. 9 Time-line plots. At the top are shown two plots of the ad-dimer position along the row as a function of time acquired at 65 and 128 C. The measured residence-time (time between hops) probability distribution at 128 C is shown at the bottom.

diffusion, 0.7 eV [31], although still substantially less than the barrier that must be overcome to remove atoms from the steps, 1.3 eV [22]. The measured prefactor, ν_0, is $10^{12.8\pm1.3}$ Hz. This value is similar to the generally accepted prefactor associated with measured metal-on-metal adatom diffusion for both simple hopping and concerted exchange displacement mechanisms [16].

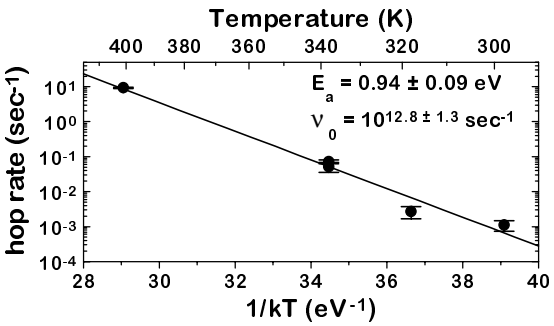

Fig. 10 Arrhenius plot of the logarithm of the diffusion rate versus 1/kT from which the activation energy barrier is extracted.

The current work demonstrates the usefulness of atom tracking in performing quantitative measurements of the self-diffusion of Si ad-dimers on the Si(001) surface as a function of temperature by substantially increasing the range of hopping rates that can be resolved. By measuring every event, it is shown that the diffusion process is simply activated and that the binding energy can be locally affected by defects. In addition to employment in atomic-scale manipulation and lithography, the ability to lock-onto and track surface dynamic events with the STM in real-time and real-space has a variety of additional important applications. Examples include studies of: surface chemical processes such as oxidation and corrosion; atomic intermixing in heterogeneous systems; electronic state evolution; as well as defect and adsorbate interactions at surfaces.

References

[1] J. F. Zheng, X. Liu, N. Newman, E. R. Weber, D. F. Ogletree, and M. Salmeron, Phys. Rev. Lett. **72**, 1490 (1994).

[2] R. M. Feenstra, J. A. Stroscio, J. Tersoff, and A. P. Fein, Phys. Rev. Lett. **58**, 1192 (1987).

[3] T. Klitsner and J. S. Nelson, Phys. Rev. Lett. **67**, 3800 (1991).

[4] P. Molinas-Mata and J. Zegenhagen, Phys. Rev. B **47**, 10319 (1993); Surf. Sci. **281**, 10 (1993).

[5] M. J. Bronikowski, Y. J. Wang, M. T. McEllistrem, D. Chen, and R. J. Hamers, Surf. Sci **298**, 50 (1993).

[6] R. M. Feenstra, J. M. Woodall, and G. D. Pettit, Phys. Rev. Lett. **71**, 1176 (1993).

[7] T. M. Lillesand and R. W. Kiefer, Remote Sensing and Image Interpretation, 3rd ed. (John Wiley and Sons, New York, 1994).

[8] R. S. Becker, B. S. Swartzentruber, J. S. Vickers, and T. Klitsner, Phys. Rev. B **39**, 1633 (1989).

[9] It is imperative that all *k* images be in registry in order for the *k*-dimensional measurement vector to be a meaningful descriptor of a given pixel, and to give reasonable classification results.

[10] This bootstrap algorithm is a generic multivariate image classification algorithm. It can also be used for satellite and medical imagery, for example.

[11] G. C. Osbourn and R. F. Martinez, Sandia National Laboratories Technical Report SAND94-0591J (1994); G. C. Osbourn, J. W. Bartholomew, G. C. Frye, and A. J. Ricco, Proc. of Sol. St. Sensors and Actuators Workshop, Hilton Head, SC, June 13-16, 1994; G.

C. Osbourn, R. F. Martinez, J. W. Bartholomew, and A. M. Bouchard, Sandia National Laboratories Technical Report SAND94-1274 (1994). (SNL Technical Reports are available upon request from the authors.)

[12] A. K. Jain and R. C. Dubes, Algorithms for Clustering Data (Prentice Hall, Englewood Cliffs, NJ, 1988).

[13] J. A. Venables, Surf. Sci., **299/300**, 798 (1994).

[14] T. Kawamura, Progress in Surf. Sci., **44**, 67 (1993).

[15] D. Srivastava and B. J. Garrison, Phys. Rev. B, **47**, 4464 (1993).

[16] G. L. Kellogg, Surf. Sci. Reports, **21**, 1 (1994).

[17] Z. Zhang, F. Wu, H. J. W. Zandvliet, B. Poelsma, H. Metiu, and M. G. Lagally, Phys. Rev. Lett., **74**, 3644 (1995).

[18] P. J. Bedrossian, Phys. Rev. Lett., **74**, 3648 (1995).

[19] R. A. Wolkow, Phys. Rev. Lett., **74**, 4448 (1995).

[20] B. S. Swartzentruber, Y. W. Mo, M. B. Webb, and M. G. Lagally, JVST A **7**, 2901 (1989).

[21] N. Kitamura, B. S. Swartzentruber, M. G. Lagally, and M. B. Webb, Phys. Rev. B, **48**, 5704 (1993).

[22] B. S. Swartzentruber and M. Schacht, Surf. Sci., **322**, 83 (1995).

[23] Many of the substrate defects also change configuration between images, some of which involve a complicated rearrangement of many atoms.

[24] D. Dijkkamp, E. J. van Loenen, and H. B. Elswijk, in *Ordering at Surfaces and Interfaces*, p. 85, eds. A. Yoshimori, T. Shinjo, and H. Watanabe (Springer-Verlag Berlin, Heidelberg 1992).

[25] For the current work we used a dither circle diameter of ~5Å at a frequency of 10 kHz. The dither amplitude must be large enough so that the convolution of the surface feature (ad-dimer) with the dither is larger than the hop length.

[26] D. W. Pohl and R. Möller, Rev. Sci. Instrum., **59**, 840 (1988).

[27] Shifting the phase of the lock-in amplifier 180 degrees enables the atom tracker to lock onto depressions.

[28] The first-generation atom tracker reported here required <25 ms to relock onto an ad-dimer's new coordinate after a diffusion event. Currently, the response time is an order of magnitude faster.

[29] see for example, J. A. Stroscio and D. M. Eigler, Science, **254**, 1319 (1991); Y. W. Mo, Science, **261**, 886 (1993); T.-C. Shen et al., Science, **268**, 1590 (1995).

[30] H. J. W. Zandvliet, unpublished, analyzed the squared-displacement distribution of Si ad-dimers on Si(001) at 340 K (380 K), and assuming a prefactor of 10^{13} Hz extracted an activation barrier of 1.02 eV (1.06 eV).

[31] Y. W. Mo, B. S. Swartzentruber, R. Kariotis, M. B. Webb, and M. G. Lagally, Phys. Rev. Lett., **63**, 2393 (1989).

Appendix

List of publications and presentations resulting from this project:

"New Method for Empirically Determining Surface Electronic Species from Multiple-Bias STM Images: A Multivariate Classification Approach", A. M. Bouchard, G. C. Osbourn, and B. S. Swartzentruber, Surf. Sci., **321**, 276 (1994). SAND94-1325J

"Direct Measurement of Surface Diffusion Using Atom-Tracking Scanning Tunneling Microscopy", B. S. Swartzentruber, Phys. Rev. Lett., **76**, 459 (1996). SAND95-1721J

"Experimental and Theoretical Study of the Rotation Rate of Si Ad-dimers on the Si(001) Surface", B. S. Swartzentruber, A. P. Smith, and H. Jónsson, Phys. Rev. Lett. **77**, 2518 (1996). SAND96-0680J

"Atomic-Scale Dynamics of Atoms and Dimers on the Si(001) Surface", B. S. Swartzentruber, 10th Toyota Conference on Atomic, Molecular, and Electronic Dynamic Processes on Surfaces, Shizuoka, Japan, November 1996. (invited) SAND96-2232A

"STM Measurements of Adsorbed Si Dimer Kinetics on Si(001)", B. S. Swartzentruber, Northern California Chapter of the American Vacuum Society, Stanford, CA, September 1996. (invited) SAND96-2224A

"Atom-Tracking STM Measurements of Si Adsorbate Diffusion and Interactions on Si(001)", B. S. Swartzentruber, 2nd Asian STM Conference, Seoul, Korea, August 1996. (invited) SAND96-1887A

"Direct Measurements of the Kinetics of Si Ad-dimers on Si(001) Using Atom-Tracking Scanning Tunneling Microscopy", B. S. Swartzentruber, TMS Annual Meeting, Anaheim, CA, February 1996. (invited) SAND95-1881A

"Measurements of Si Ad-dimer Kinetics on Si(001) Using Atom-Tracking STM", B. S. Swartzentruber, International Workshop on Nano-scale Science on Surfaces and Interfaces, Sendai, Japan, January 1996. (invited) SAND96-0177A

"Direct Measurements of the Kinetics of Si Ad-dimers on Si(001) Using Atom-Tracking STM", B. S. Swartzentruber, Fall Meeting of the Materials Research Society, Boston, MA, December 1995. SAND95-1411A

"New Method for Distinguishing Atomic or Electronic Species from Multiple-Bias STM Images", A. M. Bouchard, G. C. Osbourn, and B. S. Swartzentruber, Annual Meeting of the American Physical Society, San Jose, CA, March 1995. SAND94-3084A

"New Method for Empirically Determining Surface Electronic Species from Multiple-Bias STM Images", A. M. Bouchard, G. C. Osbourn, and B. S. Swartzentruber, 6th Annual Joint Meeting of

the New Mexico Sections of the American Ceramic Society and Materials Research Society, Albuquerque, NM, October 1994. SAND94-2318A

"New Method for Empirically Determining Surface Electronic Species from Multiple-Bias STM Images: A Multivariate Classification Approach", A. M. Bouchard, G. C. Osbourn, and B. S. Swartzentruber, Annual Meeting of the American Vacuum Society, Denver, CO, October, 1994. SAND94-1325A

List of invention disclosures: None

List of patents: None

List of copyrights: None

Information regarding employee recruitment: N/A

Information regarding involvement of post-docs in the project: This project partially supported a post-doctoral staff member, Ed J. Heller. Heller was involved in the initial construction of an STM system for studies involving chemical recognition in heterogeneous materials.